

H. Harbrecht^a · M. Randrianarivony^b

Wavelet BEM on molecular surfaces — solvent excluded surfaces

Stuttgart, June 2010

^a Institute of Applied Analysis and Numerical Simulation, University of Stuttgart,
Pfaffenwaldring 57, 70569 Stuttgart / Germany
harbrecht@ians.uni-stuttgart.de
www.ians.uni-stuttgart.de

^b Institut für Numerische Simulation, Universität Bonn,
Wegelerstr. 6, 53115 Bonn / Germany
peters@ins.uni-bonn.de
www.ins.uni-bonn.de

Abstract The present paper is concerned with to the rapid solution of a boundary integral equation for the apparent surface charge which arises from solvation continuum models. In order to apply the wavelet Galerkin scheme the molecular surface needs to be represented as a parametric surface consisting of smooth four-sided patches. We develop an algorithm which decomposes a solvent excluded surface into a set of globally continuous four-sided NURBS patches. Numerical experiments are carried out to demonstrate the feasibility and scope of the present approach.

Keywords Quantum chemistry · molecular surface · geometric modeling · wavelets · boundary element method

1 Introduction

Continuum solvation models are widely used to model quantum effects of molecules in liquid solutions. One model is widely known as the *polarizable continuum model* (PCM), introduced in [26]. In this model, the molecule under study (the solute) is located inside a cavity Ω , surrounded by a homogeneous dielectric (the solvent). The solute-solvent interactions between the charge distributions which compose the solute and the dielectric are reduced to those of electrostatic origin.

The two central components of the model are the cavity construction and the solution of the electrostatic problem. The cavity is generally constructed as a set of interlocking spheres which leads to the *van der Waals surface* (VWS) or the *solvent accessible surface* (SAS). A more elaborate but also more accurate description employs the Connolly surface in order to faithfully represent the *solvent excluded surface* (SES) by “rolling” a sphere representing a solvent molecule over the cavity [7, 8].

A convenient approach to resolve the electrostatic problem is provided by the reformulation as a boundary integral equation [5], also known as the *integral equation formalism* (IEF-PCM). In this way it is actually possible to apply the method to all cases where the Green’s function for the considered environment is known. This has been done for liquid crystals (anisotropic permittivity) [6], ionic solution (screened electrostatic potential) [5], sharp planar interfaces (image-charge approach) and diffuse planar interfaces (numerical integration) [14].

Boundary integral equations are in general solved by the boundary element method (BEM). BEM is a well established tool in PCM [5, 14, 37]. However, traditional discretizations lead to densely populated and ill-conditioned system matrices. Both features pose serious obstructions to the efficient numerical treatment of such problems. Modern methods for the rapid BEM solution reduce the complexity to almost or even optimal rates. Prominent examples for such methods are the *fast multipole method* [16], the *panel clustering* [18], *\mathcal{H} -matrices* [17], or the *wavelet Galerkin scheme* [3, 10, 22]. A Galerkin discretization with wavelet bases results in quasi-sparse matrices, i.e., the most matrix entries are negligible and can be treated as zero. Therefore, we arrive at an algorithm which solves a given boundary integral equation within discretization error accuracy, offered by the underlying Galerkin method, at a computational expense that is proven to stay proportional to the number of unknowns [10]. The method has been applied successfully to PCM in [39].

Nevertheless, the definition of the wavelets requires a parametric description of the surface by four-sided patches [19, 21, 22]. This surface representation is in contrast to the usual approximation of the surface by panels, e.g. [9, 24, 28, 29, 34]. In [20, 30, 32] an algorithm has been developed which decomposes a VWS or SAS surface into four-sided patches generated by rational Bézier surfaces. Whereas, in the present paper we will construct a parametric description of the molecule’s SES surface by a set of globally continuous four-sided NURBS patches. Besides the more accurate modelling, SES surfaces and thus the solutions of the boundary integral equation are smooth. Therefore, as supported by the numerical experiments, a piecewise bilinear boundary element method is superior to the standard approximation by piecewise constants.

This paper is organized as follows. In the next section, we give an introduction to IEF-PCM and its wavelet based fast solution. We provide basic material from geometric modeling and formulate the requirements to be fulfilled by the parametrization. In Sect. 3, we represent the SES surface by trimmed surfaces. The decomposition of these trimmed surfaces into four-sided patches will be the purpose of Sect. 4. Afterwards, in Sect. 5, we derive the representation of the patches in terms of globally continuous NURBS surfaces. Finally, we present results of our implementation where the molecular data come from real PDB files.

2 Preliminaries and problem formulation

2.1 Governing equation

In quantum chemical simulations we are seeking the electronic wave function $\Psi : \mathbb{R}^{3N} \rightarrow \mathbb{R}$ (N denotes the number of nuclei) such that the Schrödinger equation $\mathbb{E}\Psi = \mathcal{H}\Psi$ holds. In case of molecules in liquid solutions, the Hamilton operator splits into

$$\mathcal{H} = \mathcal{H}_{\text{vacuum}} + \mathcal{H}_{\text{correction}}. \quad (1)$$

The correction term $\mathcal{H}_{\text{correction}}$ incorporates the solute-solvent interactions which are reduced to those of electrostatic origin.

We shall consider a cavity Ω with boundary $\Gamma := \partial\Omega$ which represents the solute-solvent interface. The solvent in the exterior of Ω is represented by a constant dielectric medium. The solute and thus the support of the wave function Ψ is assumed to be contained inside the cavity. Therefore, the correction term in (1) refers to the interaction energy between charges ρ, ρ' , located inside the cavity Ω . It is given by

$$E_I(\rho, \rho') = \int_{\mathbb{R}^3} u(\mathbf{x})\rho'(\mathbf{x})d\mathbf{x} \quad (2)$$

with the electrostatic potential u satisfying the following transmission problem:

$$\begin{aligned} -\Delta u_i &= \rho && \text{in } \Omega, \\ -\operatorname{div}(\underline{\varepsilon}\nabla u_e) + \underline{\varepsilon}\kappa^2 u_e &= 0 && \text{in } \Omega^c := \mathbb{R}^3 \setminus \overline{\Omega}, \\ u_i &= u_e, \langle \nabla u_i, \mathbf{n} \rangle = \langle \underline{\varepsilon}\nabla u_e, \mathbf{n} \rangle && \text{on } \Gamma := \partial\Omega, \\ |u_e(\mathbf{x})| &= \mathcal{O}(\|\mathbf{x}\|^{-1}) && \text{as } \|\mathbf{x}\| \rightarrow \infty. \end{aligned} \quad (3)$$

Herein, κ accounts for the ion screening and $\underline{\varepsilon}$ is the macroscopic dielectric constant of the solvent outside Ω . In praxis, if $\underline{\varepsilon}$ is a scalar, the case of $\kappa = 0$ refers to standard PCM [26] while $\kappa \neq 0$ models ionic solutions. An anisotropic dielectric matrix $\underline{\varepsilon} \in \mathbb{R}^{3 \times 3}$ and $\kappa = 0$ applies for liquid crystals [5].

2.2 Apparent surface charge

In order to compute the interaction energy (2), we shall introduce some boundary integral operators. Associated with the interior of the cavity Ω , define the single and double layer operator of the Poisson equation

$$(\mathcal{V}_i u)(\mathbf{x}) = \int_{\Gamma} \frac{u(\mathbf{y})}{4\pi\|\mathbf{x} - \mathbf{y}\|} d\mathbf{y}, \quad (\mathcal{K}_i u)(\mathbf{x}) = \int_{\Gamma} \frac{\langle \mathbf{n}(\mathbf{y}), \mathbf{x} - \mathbf{y} \rangle}{4\pi\|\mathbf{x} - \mathbf{y}\|^3} u(\mathbf{y}) d\mathbf{y}, \quad \mathbf{x} \in \Gamma$$

and the related Newton potential

$$\mathcal{N}_\rho(\mathbf{x}) = \int_{\Omega} \frac{\rho(\mathbf{y})}{4\pi\|\mathbf{x} - \mathbf{y}\|} d\mathbf{y}, \quad \mathbf{x} \in \mathbb{R}^3. \quad (4)$$

For the exterior of the cavity, the corresponding operators associated with the linearized Poisson-Boltzmann equation are

$$\left. \begin{aligned} (\mathcal{V}_e u)(\mathbf{x}) &= \int_{\Gamma} \frac{u(\mathbf{y})e^{-\kappa\|\mathbf{x} - \mathbf{y}\|}}{4\pi\underline{\varepsilon}\|\mathbf{x} - \mathbf{y}\|} d\mathbf{y} \\ (\mathcal{K}_e u)(\mathbf{x}) &= \int_{\Gamma} \frac{\langle \mathbf{n}(\mathbf{y}), \mathbf{x} - \mathbf{y} \rangle (1 + \kappa\|\mathbf{x} - \mathbf{y}\|) e^{-\kappa\|\mathbf{x} - \mathbf{y}\|}}{4\pi\|\mathbf{x} - \mathbf{y}\|^3} u(\mathbf{y}) d\mathbf{y} \end{aligned} \right\} \quad \mathbf{x} \in \Gamma.$$

In case of an anisotropic solvent there holds

$$\left. \begin{aligned} (\mathcal{V}_e u)(\mathbf{x}) &= \int_{\Gamma} \frac{u(\mathbf{y})}{4\pi\sqrt{\det(\underline{\varepsilon})}\|\mathbf{x} - \mathbf{y}\|_{\underline{\varepsilon}^{-1}}} d\mathbf{y} \\ (\mathcal{K}_e u)(\mathbf{x}) &= \int_{\Gamma} \frac{\langle \mathbf{n}(\mathbf{y}), \mathbf{x} - \mathbf{y} \rangle}{4\pi\|\mathbf{x} - \mathbf{y}\|_{\underline{\varepsilon}^{-1}}^3} u(\mathbf{y}) d\mathbf{y} \end{aligned} \right\} \quad \mathbf{x} \in \Gamma,$$

where $\|\mathbf{x} - \mathbf{y}\|_{\underline{\varepsilon}^{-1}} := \sqrt{\langle \mathbf{x} - \mathbf{y}, \underline{\varepsilon}^{-1}(\mathbf{x} - \mathbf{y}) \rangle}$. Notice that $\mathcal{V}_{i/e} : H^{-1/2}(\Gamma) \rightarrow H^{1/2}(\Gamma)$ is symmetric and positive definite, whereas $\mathcal{K}_{i/e} : H^{1/2}(\Gamma) \rightarrow H^{1/2}(\Gamma)$ is compact, see [35].

Following [5], the sought interaction energy (2) can be expressed in terms of an *apparent surface charge* $\sigma \in H^{-1/2}(\Gamma)$.

Theorem 1 *The interaction energy between two charges $\rho, \rho' \in H^{-1}(\Omega)$ is given by*

$$E_I(\rho, \rho') = \underbrace{\int_{\mathbb{R}^3} \int_{\mathbb{R}^3} \frac{\rho(\mathbf{x})\rho'(\mathbf{y})}{4\pi\|\mathbf{x}-\mathbf{y}\|} d\mathbf{x}d\mathbf{y}}_{\text{exchange energy in the vacuum}} + \underbrace{\int_{\Gamma} \int_{\mathbb{R}^3} \frac{\rho'(\mathbf{x})\sigma(\mathbf{y})}{4\pi\|\mathbf{x}-\mathbf{y}\|} d\mathbf{x}d\mathbf{y}}_{\text{correction term: } (\sigma, N_{\rho'})_{L^2(\Gamma)}},$$

where the apparent surface charge $\sigma = \mathcal{V}_i^{-1}(u_i - \mathcal{N}_\rho) \in H^{-1/2}(\Gamma)$ satisfies the boundary integral equation

$$\left(\left(\frac{1}{2} - \mathcal{K}_e \right) \mathcal{V}_i + \mathcal{V}_e \left(\frac{1}{2} + \mathcal{K}_i^* \right) \right) \sigma = \left(\mathcal{V}_e \mathcal{V}_i^{-1} \left(\frac{1}{2} - \mathcal{K}_i \right) - \left(\frac{1}{2} - \mathcal{K}_e \right) \right) \mathcal{N}_\rho \quad \text{on } \Gamma. \quad (5)$$

Proof. Using the Dirichlet-to-Neumann maps [35]

$$\mathcal{V}_i \frac{\partial u_i}{\partial \mathbf{n}} = \left(\frac{1}{2} + \mathcal{K}_i \right) u_i - \mathcal{N}_\rho, \quad \mathcal{V}_e \langle \underline{\varepsilon} \nabla u_e, \mathbf{n} \rangle = \left(\mathcal{K}_e - \frac{1}{2} \right) u_e \quad \text{on } \Gamma$$

together with the jump conditions (3) and resolving for $\sigma := \mathcal{V}_i^{-1}(u_i - \mathcal{N}_\rho)$ yields immediately (5). The quantity σ is the sought apparent surface charge since

$$\begin{aligned} E_I(\rho, \rho') &= \int_{\mathbb{R}^3} \mathcal{N}_\rho(\mathbf{x})\rho'(\mathbf{x})d\mathbf{x} + \int_{\mathbb{R}^3} \rho'(\mathbf{x})(\mathcal{V}_i\sigma)(\mathbf{x})d\mathbf{x} \\ &= \int_{\mathbb{R}^3} \mathcal{N}_\rho(\mathbf{x})\rho'(\mathbf{x})d\mathbf{x} + \int_{\mathbb{R}^3} \rho'(\mathbf{x})\{u(\mathbf{x}) - \mathcal{N}_\rho(\mathbf{x})\}d\mathbf{x} = \int_{\mathbb{R}^3} \rho'(\mathbf{x})u(\mathbf{x})d\mathbf{x}. \end{aligned}$$

□

Remark 1 *In case of original PCM, i.e., $\kappa = 0$ and $\underline{\varepsilon}$ being a scalar, it holds $\underline{\varepsilon}\mathcal{V}_i = \mathcal{V}_e$ and $\mathcal{K}_i = \mathcal{K}_e$. Consequently, (5) can be simplified to a first kind integral equation*

$$\mathcal{V}_i\sigma = \frac{1}{\underline{\varepsilon} - 1} \mathcal{A}^{-1} \mathcal{N}_\rho - \mathcal{N}_\rho, \quad \mathcal{A} := \frac{\underline{\varepsilon} - 1}{2(\underline{\varepsilon} + 1)} - \mathcal{K}_i, \quad \text{on } \Gamma. \quad (6)$$

Since \mathcal{N}_ρ is harmonic in Ω^c , there holds

$$\mathcal{V}_i \frac{\partial \mathcal{N}_\rho}{\partial \mathbf{n}} = \left(\mathcal{K}_i - \frac{1}{2} \right) \mathcal{N}_\rho \quad \text{on } \Gamma.$$

Thus, the above integral equation can be rewritten to the second kind integral equation

$$\mathcal{A}^* \sigma = \frac{\partial \mathcal{N}_\rho}{\partial \mathbf{n}} \quad \text{on } \Gamma. \quad (7)$$

2.3 Wavelet BEM

The boundary integral equation (5) is in general numerically solved by the boundary element method (BEM). Nevertheless, traditional discretizations will lead to very large linear systems with densely populated and ill-conditioned matrices. This makes the computation very costly in both respects, the computing time and memory requirements. We shall employ a discretization by wavelets which leads to quasi-sparse matrices [3, 10].

The wavelet construction starts with a hierarchy of nested trial spaces

$$\{0\} := V_{-1} \subset V_0 \subset V_1 \subset V_2 \subset \dots, \quad V_j = \text{span}\{\varphi_{j,k} : k \in \Delta_j\}.$$

Instead of using only a single-scale j , a wavelet method is a multiscale method and keeps track of the increment of information between two adjacent scales j and $j + 1$. Since $V_{j-1} \subset V_j$ one decomposes $V_j = V_{j-1} \oplus W_j$ with some complementary space

$$W_j = \text{span}\{\psi_{j,k} : k \in \nabla_j := \Delta_j \setminus \Delta_{j-1}\},$$

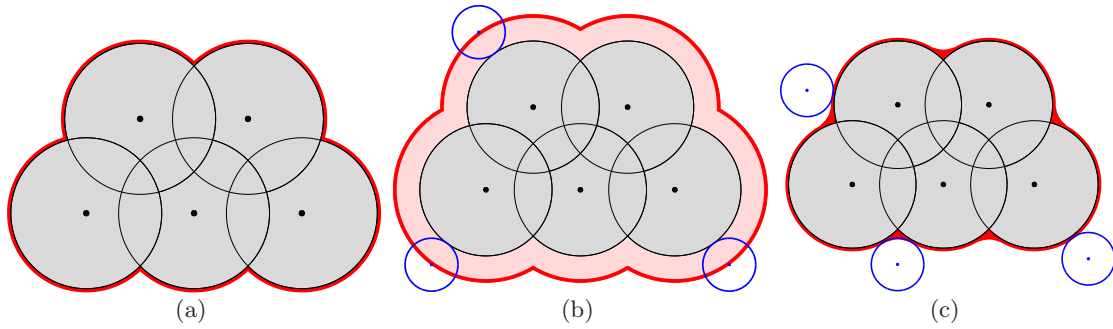


Fig. 1 (a) VWS surface, (b) SAS surface, (c) SES surface.

not necessarily orthogonal to V_{j-1} . Recursively one obtains the multiscale decomposition $V_j = \bigoplus_{\ell=0}^j W_\ell$ and thus the wavelet basis $\Psi_j = \{\psi_{\ell,k}\}_{k \in \nabla_\ell, \ell \leq j}$. Here, we respectively use piecewise constant and bi-linear wavelets with three and four vanishing moments as constructed in [21].

The boundary integral equation (5) is then discretized as follows. We make the ansatz

$$\sigma \approx \sigma \Psi_j = \sum_{\ell < j} \sum_{k \in \nabla_\ell} \sigma_{\ell,k} \psi_{\ell,k}$$

and introduce the system matrices

$$\mathbf{G} = \langle \Psi_j, \Psi_j \rangle, \quad \mathbf{V}_a = \langle \mathcal{V}_a \Psi_j, \Psi_j \rangle, \quad \mathbf{K}_a = \langle \mathcal{K}_a \Psi_j, \Psi_j \rangle, \quad a = \{i, e\}.$$

Then, the boundary integral equation (5) corresponds to the linear system of equations

$$\left(\left(\frac{1}{2} \mathbf{I} - \mathbf{K}_e \mathbf{G}^{-1} \right) \mathbf{V}_i + \mathbf{V}_e \left(\frac{1}{2} \mathbf{I} + \mathbf{G}^{-1} \mathbf{K}_i^* \right) \right) \sigma = \left(\mathbf{V}_e \mathbf{V}_i^{-1} \left(\frac{1}{2} \mathbf{G} - \mathbf{K}_i \right) - \left(\frac{1}{2} \mathbf{G} - \mathbf{K}_e \right) \right) \mathbf{f}$$

with $\mathbf{f} = \langle \mathcal{N}_\rho, \Psi_j \rangle$ being the data vector.

The Galerkin matrices are quasi-sparse in wavelet coordinates. In fact, the number of significant coefficients scales only linearly with the number of ansatz functions. Applying the matrix compression strategy developed in [10] combined with an exponentially convergent hp -quadrature method [22], the wavelet Galerkin scheme produces the approximate solution of (5) within linear complexity. Especially, due to the norm equivalences of wavelet bases, scaling the wavelets with respect to the $H^{-1/2}(\Gamma)$ -norm yields a well-conditioned system [11].

2.4 Molecular surfaces

Let $\{\mathbf{m}_k\}$ be the nuclei positions of the molecule's atoms and $\{r_k\}$ the related van der Waals radii [40]. Then, the *van der Waals surface* (VWS) corresponds to the boundary of a set of interlocking spheres

$$\Gamma_{VWS} = \partial \left(\bigcup_{k=1}^N B(\mathbf{m}_k, r_k) \right), \quad B(\mathbf{m}_k, r_k) := \{\mathbf{x} \in \mathbb{R}^3 : \|\mathbf{m}_k - \mathbf{x}\| \leq r_k\}, \quad (8)$$

see Fig. 1(a). Whereas, the *solvent accessible surface* (SAS) coincides with the VWS surface except for the scaling of the radii $\Gamma_{SAS} = \partial \left(\bigcup_{k=1}^N B(\mathbf{m}_k, r_k + \rho) \right)$, where ρ is the probe radius associated with the solvent, cf. Fig. 1(b).

We shall focus here on *solvent excluding surfaces* (SES), also known as Connolly surfaces [8]. They are derived from the VWS model by rolling a spherical probe over the surface as illustrated in Fig. 1(c). Throughout the paper, we shall make some assumptions concerning the nuclei positions \mathbf{m}_k , the radii r_k , and the probe radius ρ . For arbitrary atoms $B(\mathbf{m}_k, r_k)$ and $B(\mathbf{m}_\ell, r_\ell)$, we assume that one of the following two conditions holds.

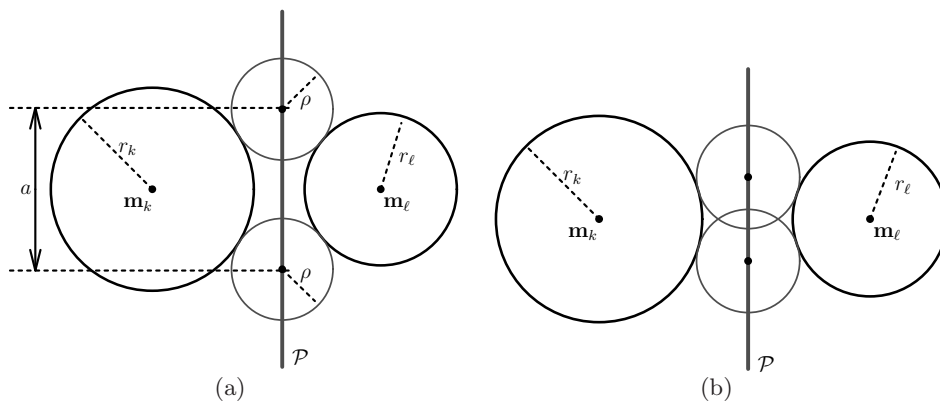


Fig. 2 (a) The interaction is admissible if $a > 2\rho$, where the plane \mathcal{P} is the radical axis of the Laguerre decomposition, (b) Inadmissible toroidal self-intersection if $a \leq 2\rho$.

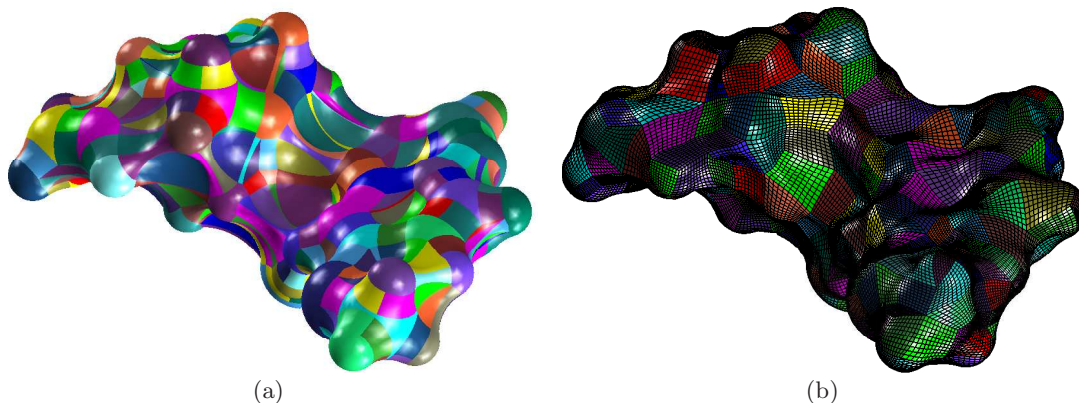


Fig. 3 SES surface of quinine with probe radius $\rho = 1.2$, represented by (a) a composition of trimmed toroidal and spherical surfaces and (b) a globally continuous NURBS parametrization.

- (C1) Either the by the probe radius ρ enlarged spheres $B(\mathbf{m}_k, r_k + \rho)$ and $B(\mathbf{m}_\ell, r_\ell + \rho)$ are completely disjoint, i.e. $\|\mathbf{m}_k - \mathbf{m}_\ell\| > r_k + r_\ell + 2\rho$,
 (C2) or we have $D_{k,\ell} := \|\mathbf{m}_k - \mathbf{m}_\ell\| \leq r_k + r_\ell + 2\rho$ and additionally

$$a := \frac{1}{D_{k,\ell}} \sqrt{4D_{k,\ell}^2(r_k + \rho)^2 - \{D_{k,\ell}^2 - (r_\ell + \rho)^2 + (r_k + \rho)^2\}^2} > 2\rho$$

(see Fig. 2(a) for an illustration of the latter relation). These assumptions exclude the situation from Fig. 2(b) where the blending torus, being tangent to $B(\mathbf{m}_k, r_k)$ and $B(\mathbf{m}_\ell, r_\ell)$, admits a self-intersection. If the assumptions (C1) or (C2) are violated but one still wants to treat the molecule, one has to insert some dummy atoms between those atoms for which there is a toroidal self-intersection [29].

Without loss of generality we assume throughout this paper that we have to deal with a single (closed) surface. The SES surface of quinine is depicted in Fig. 3.

Remark 2 In chemical applications, the radius of the probe atom is usually chosen between 1.0 \AA and 3.0 \AA but for our method it can be any positive number. When the probe radius becomes very large,

some of the initial atoms might be completely buried inside the whole surface as observed in Fig. 5(d). When the probe radius approaches zero, then the SES surface tends to the Van der Waals surface, seen in Fig. 5(a).

2.5 NURBS curves and surfaces

Since we intend to use NURBS as representation of the SES surface, let us introduce B-splines. Consider a constant integer $k \geq 2$ which specifies the smoothness of the spline and a knot sequence $\zeta_0 \leq \zeta_1 \leq \dots \leq \zeta_{n+k}$ such that $\zeta_{i+k} \neq \zeta_i$. The B-spline basis functions [23] with respect to the knot sequence $\{\zeta_i\}_i$ satisfy

$$N_i^1(t) := \begin{cases} 1, & \text{if } t \in [\zeta_i, \zeta_{i+1}), \\ 0, & \text{otherwise,} \end{cases} \quad (9)$$

and for $k = 2, 3, \dots$ the recurrence formula

$$N_i^k(t) := \left(\frac{t - \zeta_i}{\zeta_{i+k-1} - \zeta_i} \right) N_i^{k-1}(t) + \left(\frac{\zeta_{i+k} - t}{\zeta_{i+k} - \zeta_{i+1}} \right) N_{i+1}^{k-1}(t). \quad (10)$$

The B-spline is called *clamped* if the k initial and the final entries of the knot sequence coincide

$$\zeta_0 = \zeta_1 = \dots = \zeta_{k-1}, \quad \zeta_{n+1} = \zeta_{n+2} = \dots = \zeta_{n+k}. \quad (11)$$

A *Non-Uniform Rational B-Spline* (NURBS) curve, having the control points $\mathbf{d}_i \in \mathbb{R}^3$ and the weights $w_i \in \mathbb{R}_{>0}$ with respect to the above knot sequence, is a parametric curve of the form

$$\mathbf{X}(t) = \frac{\sum_{i=0}^n w_i \mathbf{d}_i N_i^k(t)}{\sum_{i=0}^n w_i N_i^k(t)}, \quad t \in [\zeta_0, \zeta_{n+k}]. \quad (12)$$

Condition (11) ensures that the first and last control point \mathbf{d}_0 and \mathbf{d}_n are interpolated. Likewise, for a NURBS surface we need two clamped knot sequences $\{\zeta_i^1\}$, $\{\zeta_j^2\}$ and associated control points $\mathbf{d}_{i,j} \in \mathbb{R}^3$ and weights $w_{i,j} \in \mathbb{R}_{>0}$. A NURBS surface is then defined as

$$\mathbf{X}(u, v) = \frac{\sum_{i=0}^n \sum_{j=0}^m w_{i,j} \mathbf{d}_{i,j} N_i^{k_1}(u) N_j^{k_2}(v)}{\sum_{i=0}^n \sum_{j=0}^m w_{i,j} N_i^{k_1}(u) N_j^{k_2}(v)}, \quad (u, v) \in [\zeta_0^1, \zeta_{n+k_1}^1] \times [\zeta_0^2, \zeta_{m+k_2}^2]. \quad (13)$$

2.6 Problem setting

The objective of the current cavity generation is to find a set of globally continuous NURBS surfaces which represents the SES surface. For each NURBS patch as in (13), we will assume that $[\zeta_0^1, \zeta_{n+k_1}^1] \times [\zeta_0^2, \zeta_{m+k_2}^2]$ is the unit square $\square := [0, 1]^2$. That is, the SES surface $\Gamma \subset \mathbb{R}^3$ will be decomposed into a finite number of patches

$$\Gamma = \bigcup_{i=1}^M \Gamma_i, \quad \Gamma_i = \gamma_i(\square), \quad i = 1, 2, \dots, M, \quad (14)$$

with $\gamma_i : \square \rightarrow \Gamma_i$ being NURBS surfaces. The intersection of two different patches Γ_i and $\Gamma_{i'}$ is supposed to be either \emptyset , or a common edge or vertex. Global continuity means that there exists a bijective, affine mapping $\Xi : \square \rightarrow \square$ such that for all $\mathbf{x} = \gamma_i(\mathbf{s})$ on a common edge of Γ_i and $\Gamma_{i'}$ it holds that $\gamma_i(\mathbf{s}) = (\gamma_{i'} \circ \Xi)(\mathbf{s})$. In other words, the NURBS functions γ_i and $\gamma_{i'}$ coincide pointwisely at common edges up to orientation.

A boundary element mesh of level j , suitable for the wavelet Galerkin scheme, is then induced by dyadic subdivisions of depth j of the unit square into 4^j cubes $C_{j,\mathbf{k}} \subset \square$, where $\mathbf{k} = (k_1, k_2)$ with $0 \leq k_1, k_2 < 2^j$. This generates $4^j M$ boundary elements $\Gamma_{i,j,\mathbf{k}} := \gamma_i(C_{j,\mathbf{k}}) \subset \Gamma_i$, $i = 1, \dots, M$. The global continuity of the parametrization ensures that the collection of elements $\{\Gamma_{i,j,\mathbf{k}}\}$ on the level j forms a regular mesh on Γ .

An instance of such a geometric processing for quinine is shown in Fig. 3(b) where the mesh refers to level 3. Observe that some patches live on the surface of several atoms. That is, one can merge some parts from different trimmed surfaces in order to form one patch. As a consequence, the size and the shape of the patches are in general very nice which is a geometric advantage of the SES surfaces over the VWS/SAS surfaces. There, each patch belongs necessarily to a single atom since the interfaces between the atoms are not smooth [20, 31].

3 Trimmed surfaces from nuclear coordinates

3.1 Laguerre decomposition

The SES surface is partly from the VWS surface Γ_{VWS} and partly from the blending surfaces traced by the probe atom. There exist only two types of blending surfaces, namely toroidal and spherical ones. Toroidal ones are generated if the probe atom touches Γ_{VWS} in two points, which is exactly the case if the probe atom rolls over the interface of two atoms. If the probe atom touches Γ_{VWS} in more than to two points, then its position is fixed and describes thus a spherical blending surface. Hence, in this section, we shall construct a boundary representation (B-Rep) of the SES surface by means of trimmed spherical and toroidal surfaces. Our starting point is a cloud of points, representing the nuclei positions, and associated radii.

First, let us introduce some nomenclature. For two spheres $\mathcal{B}_1 := \partial B(\mathbf{m}_1, r_1)$ and $\mathcal{B}_2 := \partial B(\mathbf{m}_2, r_2)$, we define the *power distance* as

$$d_{\text{pow}}(\mathcal{B}_1, \mathcal{B}_2) := \|\mathbf{m}_1 - \mathbf{m}_2\|^2 - r_1^2 - r_2^2. \quad (15)$$

This distance coincides with the usual Euclidean distance if points are supposed to be spheres of radius zero. Two spheres are called *orthogonal* if we have $d_{\text{pow}}(\mathcal{B}_1, \mathcal{B}_2) = 0$.

Let $\Delta \subset \mathbb{R}^d$ be a simplex which is a segment (resp. triangle, tetrahedron) if it is of dimension $d = 1$ (resp. $d = 2, d = 3$). Suppose that the vertices of Δ are the spheres $\mathcal{B}_i = \partial B(\mathbf{m}_i, r_i)$, $i = 0, 1, \dots, d$. The *orthosphere* of Δ is defined as the smallest sphere b such that the orthogonality relation $d_{\text{pow}}(\mathcal{B}_i, b) = 0$ holds for all $i = 0, 1, \dots, d$. The center and the radius of an orthosphere are termed *orthocenter* and *orthoradius*.

Consider a set of spheres \mathcal{B}_i , $i = 1, \dots, N$, distributed in the space \mathbb{R}^3 . The i -th *Laguerre cell* \mathcal{Z}_i is composed of all points which are closer to the sphere \mathcal{B}_i than to any other sphere \mathcal{B}_j ($j \neq i$) relative to the power distance, that is

$$\mathcal{Z}_i := \{\mathbf{x} \in \mathbb{R}^3 : d_{\text{pow}}(B(\mathbf{x}, 0), \mathcal{B}_i) \leq d_{\text{pow}}(B(\mathbf{x}, 0), \mathcal{B}_j) \ \forall j \neq i\}. \quad (16)$$

The union of all Laguerre cells defines a non-overlapping domain decomposition of \mathbb{R}^3 , i.e.,

$$\mathbb{R}^3 = \bigcup_{i=1}^N \mathcal{Z}_i, \quad \text{where } \mathcal{Z}_i^\circ \cap \mathcal{Z}_j^\circ = \emptyset \text{ if } i \neq j, \quad (17)$$

called the *Laguerre decomposition*. Notice that the Laguerre decomposition coincides with the common Voronoi decomposition if all radii are equal.

For two spheres \mathcal{B}_i and \mathcal{B}_j the *radical axis* is the set of points which are equidistant to \mathcal{B}_i and \mathcal{B}_j relative to the power distance, cf. Fig. 2. According to (15), it is given by

$$R(\mathcal{B}_i, \mathcal{B}_j) = \{\mathbf{x} \in \mathbb{R}^3 : 2\langle \mathbf{x}, \mathbf{m}_i - \mathbf{m}_j \rangle = \|\mathbf{m}_i\|^2 - \|\mathbf{m}_j\|^2 + r_j^2 - r_i^2\}. \quad (18)$$

Thus, a Laguerre cell is a possibly unbounded, convex polyhedron with faces from the radical axes. Its direct computation via (16) or (18) is too expensive. Instead, for the centers $\mathbf{m}_i = (x_i, y_i, z_i)$, the uplifting function $\tilde{\mathbf{m}}_i := (x_i, y_i, z_i, x_i^2 + y_i^2 + z_i^2 + r_i^2) \in \mathbb{R}^4$ is employed. One generates the convex hull \mathcal{H} of the set of the four dimensional points $\{\tilde{\mathbf{m}}_i\}$. The orthogonal projection of the faces of \mathcal{H} back onto the space \mathbb{R}^3 generates a weighted Delaunay tetrahedral decomposition having the apices \mathbf{m}_i . The Laguerre decomposition is obtained as the dual of the weighted Delaunay mesh, i.e., the orthocenters of these tetrahedra are the apices of the Laguerre cells. We refer the reader to [12, 15].

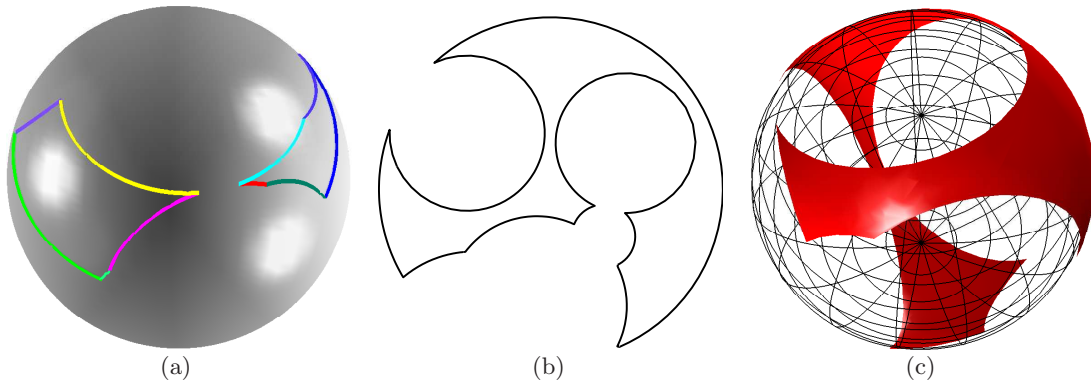


Fig. 4 (a) Circular arcs traced on atoms to form closed curves, (b) Spherical patch with composite circular arc as boundary, (c) Spherical trimmed surface.

3.2 Surface tessellation

Having the Laguerre decomposition at hand, we are able to generate those parts of the SES surface which coincide with Γ_{VWS} , given by (8). For an arbitrary atom $\mathcal{B}_k = \partial B(\mathbf{m}_k, r_k)$, we describe the way of obtaining its spherical trimmed surfaces by considering its Laguerre cell \mathcal{Z}_k . For each neighboring cell \mathcal{Z}_j , one computes two offset planes \mathcal{P}_k and \mathcal{P}_j by shifting the radical axis $R(\mathcal{B}_k, \mathcal{B}_j)$ (cf. (18)) by $d_k := D_{k,j}\rho/(r_k + \rho)$ and $d_j := D_{k,j}\rho/(r_j + \rho)$ towards the centers \mathbf{m}_k and \mathbf{m}_j , respectively. Two circles \mathcal{C}_k and \mathcal{C}_j are traced on the spheres \mathcal{B}_k and \mathcal{B}_j by these planes.

On the sphere \mathcal{B}_k , we collect all such circles $\mathcal{C}_k^1, \dots, \mathcal{C}_k^M$. The mutual intersections of the circles $\{\mathcal{C}_k^q\}$ generate cut points which decompose the circles into circular arcs. We discard the circular arcs on \mathcal{B}_k which are either contained inside another atom or beyond a plane \mathcal{P}_i . By organizing the remaining circular arcs as illustrated in Fig. 4(a), we obtain several closed curves $\mathcal{K}_1, \dots, \mathcal{K}_R$ on the sphere \mathcal{B}_k . We need then to trim off the non-relevant spherical parts which are bounded by these curves. Afterwards, we obtain on the sphere \mathcal{B}_k one or several spherical trimmed surfaces. Each of them might be simply or multiply connected.

Now, let us summarize the process of obtaining the blending surfaces which are of two types as seen in Fig. 5. The first type appears when the probe atom exactly touches two atoms. Each face $R(\mathcal{B}_k, \mathcal{B}_j)$ of the Laguerre decomposition gives rise to one torus $\mathcal{T}_{k,j}$ which is never be a horn torus or a spindle one because of the assumptions (C1) and (C2). It is a ring torus of the radius ρ . The torus $\mathcal{T}_{k,j}$ is tangent upon \mathcal{B}_k and \mathcal{B}_j where the touch-curves are the circles \mathcal{C}_k and \mathcal{C}_j as defined above. Slicing the torus $\mathcal{T}_{k,j}$ along the curves \mathcal{C}_k and \mathcal{C}_j gives rise to two toroidal components. To obtain the toroidal surface \mathbf{T} , we trim off the toroidal component which is away from the main axis of $\mathcal{T}_{k,j}$.

The second type of blending surfaces are spherical surfaces which appear if the probe atom touches at least three atoms. The radius of the blending sphere is ρ and the center is uniquely determined by at least three adjacent spheres \mathcal{B}_i , \mathcal{B}_j and \mathcal{B}_k . The boundary of each spherical blend is composed of circular arcs which are intersections with adjacent toroidal surfaces.

The main focus in the implementation of the above algorithm should be spend on its robustness. Depending on the position and the distribution of the atoms, it is possible that some circular arcs are quite tiny, as seen in Fig. 4(a). On the one hand, this leads to very long and tight toroidal blending surfaces. On the other hand, due to round-off errors, there might be gaps between the circular arcs which need to be repaired.

3.3 Homogeneous coordinates

Homogeneous coordinates are a very useful tool because rational quantities become polynomial ones which make problems linear instead of nonlinear. An element of the *projective space* \mathbb{E}^3 will be denoted as a column vector with four coordinates or as row vector whose elements are separated by

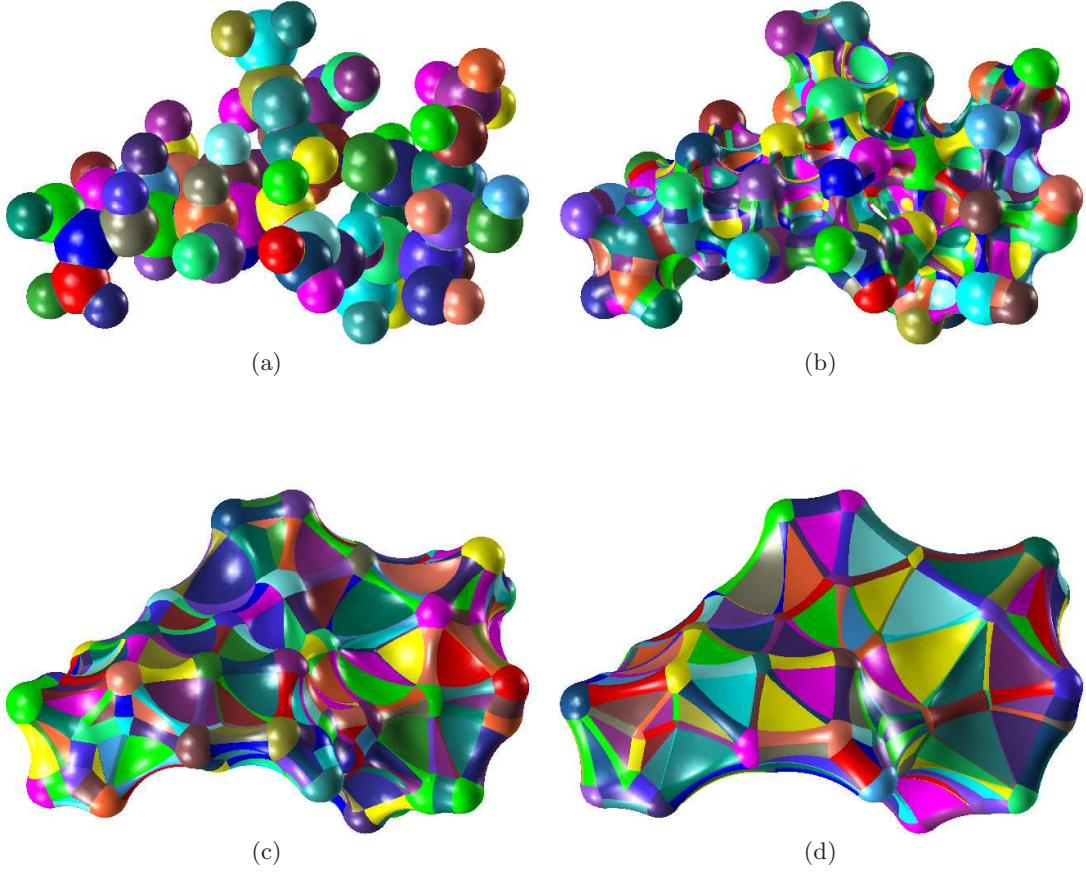


Fig. 5 B-rep of streptomycin for different probe radii: (a) 0.025 Å, (b) 0.65 Å, (c) 1.5 Å, (d) 3.0 Å.

colons. A point with *homogeneous coordinates* $[\omega : x : y : z]$ corresponds to the Cartesian coordinates $(x/\omega, y/\omega, z/\omega)$. Notice that the homogeneous coordinates $[\omega : x : y : z]$ and $[\lambda\omega : \lambda x : \lambda y : \lambda z]$ represent for any $\lambda \neq 0$ the same point in Cartesian coordinates.

In homogeneous coordinates, the NURBS curve (12) becomes a B-spline curve with coefficients $[\omega_i : \omega_i d_{i,1} : \omega_i d_{i,2} : \omega_i d_{i,3}]$, i.e.,

$$\mathbf{X}(t) = \sum_{i=0}^n [\omega_i : \omega_i d_{i,1} : \omega_i d_{i,2} : \omega_i d_{i,3}] N_i^k(t).$$

Vice versa, the homogeneous B-spline curve $\mathbf{X}(t) = \sum_{i=0}^n [\alpha_i : \beta_i : \gamma_i : \delta_i] N_i^k(t)$ corresponds uniquely (except for scaling of numerator and denominator) to a NURBS curve (12) with $\omega_i := \alpha_i$ and $\mathbf{d}_i := (\beta_i/\alpha_i, \gamma_i/\alpha_i, \delta_i/\alpha_i)$. Likewise, a NURBS surface $\mathbf{X}(\cdot, \cdot)$ (13) which has the control points $\mathbf{d}_{i,j} = (x_{i,j}, y_{i,j}, z_{i,j})$ and the weights $\omega_{i,j}$ (for $i = 0, 1, \dots, n$ and $j = 0, 1, \dots, m$) can be represented in homogeneous coordinates as

$$\mathbf{X}(u, v) = \sum_{i=0}^n \sum_{j=0}^m [\omega_{i,j} : \omega_{i,j} x_{i,j} : \omega_{i,j} y_{i,j} : \omega_{i,j} z_{i,j}] N_i^{k_1}(u) N_j^{k_2}(v).$$

3.4 Stereographic projection

As seen in Subsect. 3.2, two instances can generate trimmed spherical patches. Namely, there are patches which have the atoms as base surface and patches which have the probe atom as base surface. In both cases, the boundaries of the spherical patches are circular arcs. To obtain a parametrization of these patches, we will employ the *stereographic projection* σ [15]. To this end, we introduce the plane

$$\mathbb{P} := \{[\omega : x : y : 0] \in \mathbb{E}^3 : \omega \neq 0\} = \{(x, y, z) \in \mathbb{R}^3 : z = 0\}$$

and the unit sphere

$$\mathbb{S}^2 := \{[\omega : x : y : z] \in \mathbb{E}^3 : \omega \neq 0, x^2 + y^2 + z^2 = \omega^2\} = \{\mathbf{x} \in \mathbb{R}^3 : \|\mathbf{x}\| = 1\}.$$

Then, the stereographic projection $\sigma : \mathbb{S}^2 \rightarrow \mathbb{P}$ maps the point $(x, y, z) = [\omega : \omega x : \omega y : \omega z] \in \mathbb{S}^2$ to

$$\sigma(x, y, z) = \left(\frac{x}{1-z}, \frac{y}{1-z}, 0 \right) = [\omega(1-z) : \omega x : \omega y : 0] \in \mathbb{P},$$

see [27]. The inverse $\tau := \sigma^{-1} : \mathbb{P} \rightarrow \mathbb{S}^2$ is given by

$$\begin{aligned} \tau(x, y, z) &= \left(\frac{2x}{x^2 + y^2 + 1}, \frac{2y}{x^2 + y^2 + 1}, \frac{x^2 + y^2 - 1}{x^2 + y^2 + 1} \right) \\ &= [\omega^2(x^2 + y^2 + 1) : 2\omega^2 x : 2\omega^2 y : \omega^2(x^2 + y^2 - 1)] \in \mathbb{S}^2. \end{aligned}$$

Suppose that the B-Spline curve $\mathbf{X} \subset \mathbb{S}^2$ is given in homogeneous coordinates by

$$\mathbf{X}(t) = \sum_{i=0}^n [\omega_i : \omega_i x_i : \omega_i y_i : \omega_i z_i] N_i^k(t)$$

with $z_i \neq 1$ for all i . Then, the stereographic projection maps $\mathbf{X}(t)$ onto

$$\mathbf{Y}(t) = \sigma(\mathbf{X}(t)) = \begin{bmatrix} \sum_{i=0}^n (\omega_i - \omega_i z_i) N_i^k(t) \\ \sum_{i=0}^n \omega_i x_i N_i^k(t) \\ \sum_{i=0}^n \omega_i y_i N_i^k(t) \\ 0 \end{bmatrix} = \begin{bmatrix} \sum_{i=0}^n \tilde{\omega}_i N_i^k(t) \\ \sum_{i=0}^n \tilde{\omega}_i \tilde{x}_i N_i^k(t) \\ \sum_{i=0}^n \tilde{\omega}_i \tilde{y}_i N_i^k(t) \\ 0 \end{bmatrix} \in \mathbb{P}$$

where $\tilde{\omega}_i := \omega_i(1 - z_i)$ and $\tilde{\mathbf{b}}_i := (\tilde{x}_i, \tilde{y}_i, 0) := (x_i/(1 - z_i), y_i/(1 - z_i), 0)$. In other words, the preimage with respect to τ of the curve of $\mathbf{X} \subset \mathbb{S}^2$ is the NURBS curve

$$\mathbf{Y}(t) = \frac{\sum_{i=0}^n \tilde{\omega}_i \tilde{\mathbf{b}}_i N_i^k(t)}{\sum_{i=0}^n \tilde{\omega}_i N_i^k(t)} \in \mathbb{P}.$$

Consequently, circular arcs and likewise spherical patches can be represented exactly by NURBS curves and patches.

3.5 Parametrizing the trimmed surfaces

As described in the previous subsections, we need to represent only two types of trimmed surfaces $\mathbf{S} \subset \Gamma_{SES}$, namely spherical and toroidal ones. They are always bounded by incident circular arcs \mathcal{C}_j with $j \in \mathcal{J}$, i.e.,

$$\partial \mathbf{S} = \bigcup_{j \in \mathcal{J}} \mathcal{C}_j.$$

In case of \mathbf{S} being a spherical surface, say $\mathbf{S} \subset \mathcal{B}$ with \mathcal{B} being an atom of the molecule or the probe atom, we shall exploit the stereographic projection σ to represent it as a parametric trimmed surface defined on some planar domain. To this end, let us denote by σ the analogue of the stereographic projection with respect to the underlying sphere \mathcal{B} . According to Subsect. 3.4, by setting $\tau := \sigma^{-1}$, we can compute the curves $\mathcal{E}_j = \tau(\mathcal{C}_j) \subset \mathbb{P}$ for each circular arc $\mathcal{C}_j \subset \mathcal{B}$ with $j \in \mathcal{J}$. Denoting by \mathbf{D}

the planar trimmed domain bounded by $\partial\mathbf{D} = \bigcup_{j \in \mathcal{J}} \mathcal{E}_j$ we thus have constructed the trimmed surface [4, 23]

$$\tau : \mathbf{D} \rightarrow \mathbf{S} \quad \text{with} \quad \mathbf{S} = \tau(\mathbf{D}) \subset \mathcal{B}.$$

Notice that the preimage by τ of a 3D circular arc is a 2D circular arc and thus representable exactly by a NURBS curve. In Fig. 4(b) the parameter domain \mathbf{D} is seen which yields via τ the trimmed surface Fig. 4(c).

Similarly to above, we can define trimmed surfaces to represent the toroidal blending surfaces. Their parametrization consists of a surface of revolution where the directrix is a circular arc. All in all, we get the final B-rep in terms of trimmed surfaces:

$$\Gamma_{SES} = \bigcup_{i=1}^N \mathbf{S}_i \quad \text{with} \quad \kappa_i : \mathbf{D}_i \rightarrow \mathbf{S}_i. \quad (19)$$

4 Decomposition into four-sided domains

4.1 Initial triangulation

In this section, we describe the decomposition of the B-rep of the SES surface into large four-sided subsurfaces. It is very difficult (if possible at all) to directly decompose the SES surface from its raw representation (19). Instead, we generate a discretization \mathcal{M} of the surface Γ_{SES} first. A convenient way of generating such a discretization is based on a triangulation which is constructed in accordance with [33].

Consider a trimmed surface

$$\kappa : \mathbf{D} \rightarrow \mathbf{S} \quad \text{with} \quad \mathbf{S} = \kappa(\mathbf{D}) \subset \Gamma_{SES}.$$

An appropriate 2D triangulation of the parameter domain \mathbf{D} is lifted to the parametric surface \mathbf{S} by computing the image of all nodes under κ . For sake of completeness we briefly introduce the approach here. To this end, we will call an edge of a mesh in the parameter domain a *2D edge* and an edge in the lifted mesh a *3D edge*.

We construct an initial triangulation of the parameter domain \mathbf{D} by approximating it as a polygon. This polygon may contain holes and is assumed to resolve the underlying topology. The initial polygon \mathcal{P} is split into a few simply connected polygons $\mathcal{P} = \bigcup_{i=1}^n \mathcal{P}^{(i)}$. Afterwards, we do the following for every simply connected polygon $\mathcal{P}^{(i)}$. One initializes its set of triangles as empty set $\mathcal{T}_h^{(i)} := \emptyset$. Then, one finds a triangle T which can be chopped off from $\mathcal{P}^{(i)}$. We can repeat this process by updating $\mathcal{P}^{(i)} := \mathcal{P}^{(i)} \setminus T$ and $\mathcal{T}_h^{(i)} := \mathcal{T}_h^{(i)} \cup T$. Finally, the triangulation of \mathcal{P} is the union of all triangulations: $\mathcal{T}_h := \bigcup_i \mathcal{T}_h^{(i)}$. Finally, the edges between adjacent boundary nodes are replaced by the boundary curve.

Next we define an edge size function $\rho : \mathbf{S} \rightarrow \mathbb{R}_{\geq 0}$ on the parametric surface \mathbf{S} via the Laplace-Beltrami equation

$$\Delta_\Gamma \rho = 0 \text{ in } \mathbf{S}, \quad \rho = \rho_{\text{bound}} \text{ on } \partial\mathbf{S}$$

where ρ_{bound} is prescribed by the above coarse triangulation. By composing ρ with the parameterization κ of \mathbf{S} , we obtain the so-called parameter edge size function $\tilde{\rho} := \rho \circ \kappa : \mathbf{D} \rightarrow \mathbb{R}_{\geq 0}$.

For all internal 2D edges we then alternate the following two operations as long as the triangulation does not change any more.

(1) If the two triangles $[\mathbf{a}, \mathbf{b}, \mathbf{c}]$ and $[\mathbf{a}, \mathbf{c}, \mathbf{d}]$ which share the edge $[\mathbf{a}, \mathbf{c}]$ form a convex quadrilateral, then the edge is flipped into $[\mathbf{b}, \mathbf{d}]$ if the following generalized Delaunay angle criterion is met

$$\|(\mathbf{a} - \mathbf{b}) \times (\mathbf{c} - \mathbf{b})\| \langle \mathbf{a} - \mathbf{d}, \mathbf{T}(\mathbf{c} - \mathbf{d}) \rangle < \|(\mathbf{a} - \mathbf{d}) \times (\mathbf{c} - \mathbf{d})\| \langle \mathbf{a} - \mathbf{b}, \mathbf{T}(\mathbf{c} - \mathbf{b}) \rangle.$$

Here, \mathbf{T} denotes the mean of the first fundamental forms $\mathbf{I}_a, \mathbf{I}_b, \mathbf{I}_c$ and \mathbf{I}_d at the nodes.

(2) An edge $[\mathbf{a}, \mathbf{b}]$ is split if the average distance

$$d_{\text{Riem}}(\mathbf{a}, \mathbf{b}) := \sqrt{\langle \mathbf{b} - \mathbf{a}, \mathbf{T}(\mathbf{b} - \mathbf{a}) \rangle} \quad \text{where} \quad \mathbf{T} := \frac{1}{2}(\mathbf{I}_a + \mathbf{I}_b).$$

exceeds the value of the parameter edge size function $\tilde{\rho}$ at the midpoint of $[\mathbf{a}, \mathbf{b}]$.

4.2 Quadrangulation

The process of generating the patches starts from a fine quadrangulation $\mathcal{Q}_{\text{fine}}$ which is obtained by subdividing each triangular element of \mathcal{M} into three quadrilaterals. More precisely, a new node is inserted at the center of gravity of each triangle and three new nodes at the midpoints of its three edges.

Pattern	Simplification

Table 1 Pattern and related simplification.

Since the resulting quadrangulation is too fine, we need to coarsen the quadrangulation. We initialize $\mathcal{Q}_0 := \mathcal{Q}_{\text{fine}}$ and apply repeatedly coarsening steps $\mathcal{Q}_k \mapsto \mathcal{Q}_{k+1}$. Each coarsening consists in amalgamating a few neighboring quadrilaterals of \mathcal{Q}_k to form a coarser in \mathcal{Q}_{k+1} . Each quadrilateral amalgamation is most easily described by using 2D patterns as seen in Tab. 1. Related simplifications, belonging to \mathcal{Q}_k , are depicted in the right column of this table. Notice that the simplifications do not change the pattern's shape.

It is beyond the scope of this paper to describe all possible simplification patterns. We implemented more than 50 different pattern which to our experience is enough to get a robust coarsening algorithm. However, when applying the patterns to quadrangulations on manifolds, geometrical conflicts like foldings or irregular mappings might occur. To check the shape property of a quadrilaterals, we investigate the Coons map resulting from the four straight boundary curves.

Once the coarse quadrangulation $\mathcal{Q}_{\text{coarse}}$ is available, we replace every edge of $\mathcal{Q}_{\text{coarse}}$ by a curve $\mathcal{E} \subset \Gamma_{SES}$ with the same endpoints. Geodesics serve as a good method to determine such curves.

4.3 Cleaning up

In many decomposition techniques, *clean-up* is the process of generating a tessellation by improving an available one according to a given quality criterion. We will keep the numbers of nodes and edges fixed but we move the position of the nodes and edges in order to enhance the quality of the quadrangulation.

Before describing the clean-up operations, let us consider a technique of assessing the quality of a convex quadrilateral. It requires the introduction of the following distortion coefficient of any triangle $[\mathbf{a}, \mathbf{b}, \mathbf{c}]$:

$$\beta := 2\sqrt{3} \frac{\|(\mathbf{c} - \mathbf{a}) \times (\mathbf{a} - \mathbf{b})\|}{\|\mathbf{c} - \mathbf{a}\|^2 + \|\mathbf{a} - \mathbf{b}\|^2 + \|\mathbf{b} - \mathbf{c}\|^2} \in [0, 1].$$

The triangular distortion satisfies $\alpha = 1$ if the triangle $[\mathbf{a}, \mathbf{b}, \mathbf{c}]$ is equilateral.

For a given convex quadrilateral $\mathcal{Q} = [\mathbf{a}, \mathbf{b}, \mathbf{c}, \mathbf{d}]$ we compute the triangular distortions β_i of the triangles $[\mathbf{a}, \mathbf{b}, \mathbf{c}]$, $[\mathbf{a}, \mathbf{c}, \mathbf{d}]$, $[\mathbf{a}, \mathbf{b}, \mathbf{d}]$ and $[\mathbf{b}, \mathbf{c}, \mathbf{d}]$. By ordering them such that $\beta_1 \geq \beta_2 \geq \beta_3 \geq \beta_4$, we

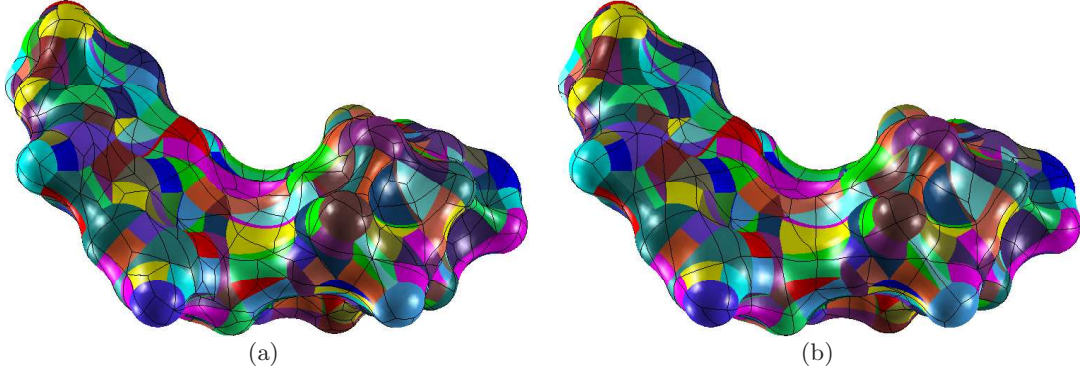


Fig. 6 Quadrangulation simplification with NND nodes, NEL quadrilaterals and NED edges: (a)NND=484, NEL=482, NND=964 (b)NND=251, NEL=249, NND=498.

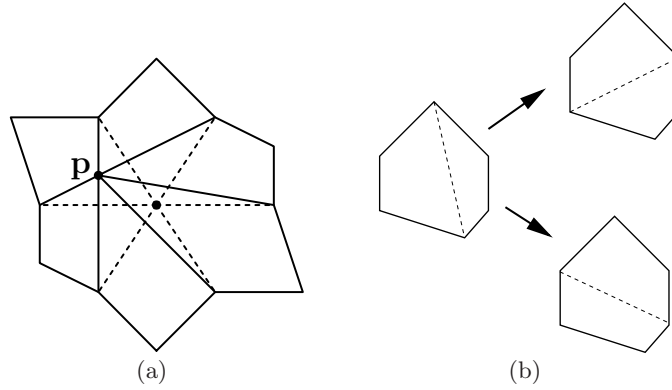


Fig. 7 Clean-up: (a) Shifting a node \mathbf{p} , (b) Flipping an edge.

can measure the quality of the quadrilateral \mathcal{Q} by

$$\mu(\mathcal{Q}) := (\beta_3\beta_4)/(\beta_1\beta_2) \in [0, 1].$$

It holds $\mu(\mathcal{Q}) = 1$ if \mathcal{Q} is a rectangle whereas $\mu(\mathcal{Q})$ becomes small as the quadrilateral becomes triangular shaped. Since a node \mathbf{p} is shared by several quadrilaterals \mathcal{Q}_j , $j \in \mathcal{J}$, its quality can be measured by

$$\mu(\mathbf{p}) := \frac{1}{\text{card}(\mathcal{J})} \sum_{j \in \mathcal{J}} \mu(\mathcal{Q}_j).$$

Similarly, the quality of common edge \mathcal{E} of the quadrilaterals \mathcal{Q}_1 and \mathcal{Q}_2 is measured by

$$\mu(\mathcal{E}) := \frac{1}{2} \{ \mu(\mathcal{Q}_1) + \mu(\mathcal{Q}_2) \}.$$

Our cleaning-up is done by alternating the following two operations several times: *node repositioning* and *edge flipping*. The first one consists in shifting an internal node to another position in order to improve the quality of the neighboring quadrilaterals. In the course of node shifting, we have to make sure that all incident quadrilaterals remain convex. The second operation modifies the endpoints of an internal edge.

The node repositioning consists in moving a node \mathbf{p} in order to minimize $\mu(\mathbf{p})$. Let us denote by e the minimal length of the edges which emanate from the node \mathbf{p} . Consider a circle centered at the node \mathbf{p} and having radius $\rho := \lambda e$ where $\lambda \in (0, 1)$ is a user defined parameter (say $\lambda = 0.25$). The new

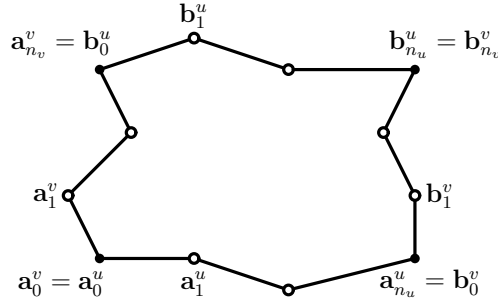


Fig. 8 Compatibility condition of the control points of the bounding curves.

position of \mathbf{p} is then sought inside this circle. The practical realization of such a shifting is to pick ℓ (say $\ell = 5$) positions \mathbf{q}_i inside the circle. For every \mathbf{q}_i we test if by replacing \mathbf{p} by \mathbf{q}_i we would still have incident nicely shaped quadrilaterals. We replace then \mathbf{p} by \mathbf{q}_i which gives new incident quadrilaterals and which minimizes $\mu(\mathbf{q}_i)$. If none of the \mathbf{q}_i fulfills the desirable properties, then we keep \mathbf{p} in its current position.

The second operation consists in flipping an edge in order to improve the qualities of the neighboring quadrilaterals. In the best case, there are two possibilities for flipping an edge by considering the union of the incident quadrilaterals as illustrated in Fig. 7(b). We flip an internal edge \mathcal{E} to a position which keeps the two incident quadrilaterals nicely shaped and which improves the value of $\mu(\mathcal{E})$.

5 Globally continuous spline representation

The objective of this section is the determination of a NURBS parametrization which is globally continuous. To this end, we are given four boundary NURBS curves

$$\begin{aligned} K_1^u(t) &= \frac{\sum_{i=0}^{n_u} \mathbf{a}_i^u w_{a,i}^u N_i^k(t)}{\sum_{i=0}^{n_u} w_{a,i}^u N_i^k(t)}, & K_2^u(t) &= \frac{\sum_{i=0}^{n_u} \mathbf{b}_i^u w_{b,i}^u N_i^k(t)}{\sum_{i=0}^{n_u} w_{b,i}^u N_i^k(t)}, \\ K_1^v(t) &= \frac{\sum_{i=0}^{n_v} \mathbf{a}_i^v w_{a,i}^v N_i^k(t)}{\sum_{i=0}^{n_v} w_{a,i}^v N_i^k(t)}, & K_2^v(t) &= \frac{\sum_{i=0}^{n_v} \mathbf{b}_i^v w_{b,i}^v N_i^k(t)}{\sum_{i=0}^{n_v} w_{b,i}^v N_i^k(t)}. \end{aligned}$$

We assume that all four curves are defined on the interval $[0, 1]$ and that the knot sequences of the opposite curves K_1^p and K_2^p for $p = u, v$ are the same. Otherwise, we insert additional knots in a preprocessing step. We further assume compatibility conditions related to the control points and weights at the corners (see Fig. 8):

$$\begin{aligned} \mathbf{a}_{n_v}^u &= \mathbf{b}_0^u, & \mathbf{a}_0^v &= \mathbf{a}_0^u, & \mathbf{a}_{n_u}^u &= \mathbf{b}_0^v, & \mathbf{b}_{n_u}^u &= \mathbf{b}_{n_v}^v, \\ \omega_{a,n_v}^u &= \omega_{b,0}^u, & \omega_{a,0}^v &= \omega_{a,0}^u, & \omega_{a,n_u}^u &= \omega_{b,0}^v, & \omega_{b,n_u}^u &= \omega_{b,n_v}^v. \end{aligned} \quad (20)$$

Suppose we are given a set of samples $(u_i, v_i) \in [0, 1]^2$ and data points $\mathbf{p}_i \in \mathbb{R}^3$ for $i = 0, 1, \dots, M$. To approximate these samples, we seek a NURBS surface

$$\gamma(u, v) = \left(\frac{x_1(u, v)}{\omega(u, v)}, \frac{x_2(u, v)}{\omega(u, v)}, \frac{x_3(u, v)}{\omega(u, v)} \right)$$

where

$$x_q(u, v) = \sum_{i=0}^{n_u} \sum_{j=0}^{n_v} w_{i,j} d_{i,j}^q N_i^{k_u}(u) N_j^{k_v}(v), \quad q = 1, 2, 3, \quad (21)$$

and

$$\omega(u, v) = \sum_{i=0}^{n_u} \sum_{j=0}^{n_v} w_{i,j} N_i^{k_u}(u) N_j^{k_v}(v) \quad (22)$$

with unknown control points $\mathbf{d}_{i,j} := (d_{i,j}^1, d_{i,j}^2, d_{i,j}^3) \in \mathbb{R}^3$ and weights $w_{i,j} \in \mathbb{R}_{>0}$. For sake of simplicity in representation we introduce the index set $\mathcal{Z} := \{\boldsymbol{\nu} = (i, j) : 0 \leq i, j \leq n\}$ and define $N_{\boldsymbol{\nu}}(u, v) := N_i^{k_u}(u)N_j^{k_v}(v)$. With the help of this new notation, (21) and (22) are equivalent to

$$x_q(u, v) = \sum_{\boldsymbol{\nu} \in \mathcal{J}} w_{\boldsymbol{\nu}} d_{\boldsymbol{\nu}}^q N_{\boldsymbol{\nu}}(u, v), \quad \omega(u, v) = \sum_{\boldsymbol{\nu} \in \mathcal{J}} w_{\boldsymbol{\nu}} N_{\boldsymbol{\nu}}(u, v), \quad q = 1, 2, 3.$$

The NURBS surface becomes in homogeneous coordinates

$$\bar{\boldsymbol{\gamma}}(u, v) = [\omega(u, v) : x_1(u, v) : x_2(u, v) : x_3(u, v)].$$

A data point $\mathbf{p} = (p_1, p_2, p_3)$ will be identified with a point in the projective space

$$\bar{\mathbf{p}} = [\beta : \beta p_1 : \beta p_2 : \beta p_3] \quad \text{with} \quad \beta(\mathbf{p}) := 1/\sqrt{1 + \|\mathbf{p}\|^2} = 1/\sqrt{1 + p_1^2 + p_2^2 + p_3^2}.$$

We follow [13] and introduce the following distance functional of the above surface to the point $\bar{\mathbf{p}}$

$$\begin{aligned} Q(\bar{\boldsymbol{\gamma}}(u, v), \bar{\mathbf{p}}) &:= \|\bar{\boldsymbol{\gamma}}(u, v)\|^2 - \langle \bar{\boldsymbol{\gamma}}(u, v), \bar{\mathbf{p}} \rangle \\ &= \omega(u, v)^2 + \sum_{q=1}^3 x_q(u, v)^2 - \beta \left[\omega(u, v) + \sum_{q=1}^3 p_q x_q(u, v) \right]^2. \end{aligned}$$

The sought NURBS surface is now the solution of the minimization problem

$$F(\{\mathbf{d}_{\boldsymbol{\nu}}\}, \{w_{\boldsymbol{\nu}}\}) := \sum_{i=0}^M Q(\bar{\boldsymbol{\gamma}}(u_i, v_i), \bar{\mathbf{p}}_i) \rightarrow \inf.$$

To avoid a NURBS function with negative or zero weights, we add a regularization term

$$\tilde{F}_{\lambda}(\{\mathbf{d}_{\boldsymbol{\nu}}\}, \{w_{\boldsymbol{\nu}}\}) := \sum_{i=0}^M \left\{ Q(\bar{\boldsymbol{\gamma}}(u_i, v_i), \bar{\mathbf{p}}_i) + \lambda R(\bar{\boldsymbol{\gamma}}(u_i, v_i)) \right\} \rightarrow \inf \quad (23)$$

where $R(\bar{\boldsymbol{\gamma}}(u_i, v_i)) := [w(u_i, v_i) - 1]^2$. As the value of the parameter λ becomes large, the weights are likely to be positive. Thus, this value is a trade-off between the approximation and the regularity. In practice, the value of λ starts from a small one and is incremented gradually until all weights are positive.

For the purpose of global continuity, the control points and weights on the boundary are interpolated while the internal ones need to be determined. Thus, the boundary entities verify

$$\begin{aligned} \mathbf{d}_{i,0} &:= \mathbf{a}_i^u, \quad \omega_{i,0} := \omega_{a,i}^u, \quad \mathbf{d}_{i,n_v} := \mathbf{b}_i^u, \quad \omega_{i,n_v} := \omega_{b,i}^u, \quad \text{for } i = 0, \dots, n_u, \\ \mathbf{d}_{0,j} &:= \mathbf{a}_j^v, \quad \omega_{0,j} := \omega_{a,j}^v, \quad \mathbf{d}_{n_u,j} := \mathbf{b}_j^v, \quad \omega_{n_u,j} := \omega_{b,j}^v, \quad \text{for } j = 0, \dots, n_v. \end{aligned}$$

Let us denote by $\mathcal{I} \subset \mathcal{J}$ the set of indices whose corresponding control points $\mathbf{d}_{\boldsymbol{\nu}}$ are internal ones. Likewise, the set of indices of the boundary control points is denoted by $\mathcal{B} := \mathcal{J} \setminus \mathcal{I}$. As for the coordinates, we define $Z(\mathcal{I}) := \{1, 2, 3\} \times \mathcal{I}$ while the set $Z(\mathcal{B})$ is defined analogously. The coordinates of the internal control points are $d_{\boldsymbol{\nu}}^q$ for $(q, \boldsymbol{\nu}) \in Z(\mathcal{I})$. We further will abbreviate $\alpha_i(\boldsymbol{\nu}_1, \boldsymbol{\nu}_2) := N_{\boldsymbol{\nu}_1}(u_i, v_i)N_{\boldsymbol{\nu}_2}(u_i, v_i)$ and $\beta_i := \beta(\mathbf{p}_i)$.

For any $(q_0, \boldsymbol{\nu}_0) \in Z(\mathcal{I})$, the partial derivative of \tilde{F}_{λ} with respect to $d_{\boldsymbol{\nu}_0}^{q_0}$ is given by

$$\frac{\partial \tilde{F}_{\lambda}}{\partial d_{\boldsymbol{\nu}_0}^{q_0}}(\{\mathbf{d}_{\boldsymbol{\nu}}\}, \{w_{\boldsymbol{\nu}}\}) = \sum_{i=0}^M \sum_{\boldsymbol{\nu} \in \mathcal{J}} \alpha_i(\boldsymbol{\nu}, \boldsymbol{\nu}_0) \left[\tilde{d}_s^{q_0} \sum_{q=1}^3 (\delta_{q,q_0} - \beta_i p_{q,i} p_{q_0,i}) - \beta_i \omega_{\boldsymbol{\nu}} p_{q_0,i} \right].$$

The partial derivative of \tilde{F}_{λ} with respect to $\omega_{\boldsymbol{\nu}_0}$ is

$$\frac{\partial \tilde{F}_{\lambda}}{\partial \omega_{\boldsymbol{\nu}_0}}(\{\mathbf{d}_{\boldsymbol{\nu}}\}, \{w_{\boldsymbol{\nu}}\}) = \sum_{i=0}^M \left\{ \sum_{\boldsymbol{\nu} \in \mathcal{J}} \alpha_i(\boldsymbol{\nu}, \boldsymbol{\nu}_0) \left[(1 + \lambda - \beta_i) \omega_{\boldsymbol{\nu}} - \beta_i \sum_{q=1}^3 p_{q,i} d_{\boldsymbol{\nu}}^q \right] - \lambda N_{\boldsymbol{\nu}_0}(u_i, v_i) \right\}.$$

Claiming that these derivatives are equal to 0, we obtain in virtue of the boundary conditions that

$$\sum_{(q,\nu) \in Z(\mathcal{I})} \left[\sum_{i=0}^M (\delta_{q,q_0} - \beta_i p_{q,i} p_{q_0,i}) \alpha_i(\boldsymbol{\nu}, \boldsymbol{\nu}_0) \right] d_{\boldsymbol{\nu}}^q - \sum_{s \in \mathcal{I}} \left[\sum_{i=0}^M \beta_i p_{q_0,i} \alpha_i(\boldsymbol{\nu}, \boldsymbol{\nu}_0) \right] \omega_{\boldsymbol{\nu}} = G_{\boldsymbol{\nu}_0}^{q_0}, \quad (24)$$

$$\sum_{(q,\nu) \in Z(\mathcal{I})} \left[\sum_{i=0}^M -\beta_i p_{q,i} \alpha_i(\boldsymbol{\nu}, \boldsymbol{\nu}_0) \right] d_{\boldsymbol{\nu}}^q + \sum_{s \in \mathcal{I}} \left[\sum_{i=0}^M (1 + \lambda - \beta_i) \alpha_i(\boldsymbol{\nu}, \boldsymbol{\nu}_0) \right] \omega_{\boldsymbol{\nu}} = H_{\boldsymbol{\nu}_0}, \quad (25)$$

where

$$\begin{aligned} G_{\boldsymbol{\nu}_0}^{q_0} &:= \sum_{(q,\nu) \in Z(\mathcal{B})} \left[\sum_{i=0}^M (\beta_i p_{q,i} p_{q_0,i} - \delta_{q,q_0}) \alpha_i(\boldsymbol{\nu}, \boldsymbol{\nu}_0) \right] d_{\boldsymbol{\nu}}^q + \sum_{s \in \mathcal{B}} \left[\sum_{i=0}^M \beta_i p_{q_0,i} \alpha_i(\boldsymbol{\nu}, \boldsymbol{\nu}_0) \right] \omega_{\boldsymbol{\nu}}, \\ H_{\boldsymbol{\nu}_0} &:= \sum_{(q,\nu) \in Z(\mathcal{B})} \left[\sum_{i=0}^M \beta_i p_{q,i} \alpha_i(\boldsymbol{\nu}, \boldsymbol{\nu}_0) \right] d_{\boldsymbol{\nu}}^q \\ &\quad - \sum_{s \in \mathcal{B}} \left[\sum_{i=0}^M (1 + \lambda - \beta_i) \alpha_i(\boldsymbol{\nu}, \boldsymbol{\nu}_0) \right] \omega_{\boldsymbol{\nu}} + \lambda \sum_{i=0}^M N_{\boldsymbol{\nu}_0}(u_i, v_i). \end{aligned}$$

Consequently, we obtain $\text{card}(Z(\mathcal{I})) + \text{card}(\mathcal{I}) = 4 \text{card}(\mathcal{I})$ linear equations for the 4 $\text{card}(\mathcal{I})$ unknowns $\{d_{\boldsymbol{\nu}}^q\}_{(\boldsymbol{\nu},q) \in Z(\mathcal{I})}$ and $\{\omega_{\boldsymbol{\nu}}\}_{\boldsymbol{\nu} \in \mathcal{I}}$.

Theorem 2 ([13]) *The linear system of equations (24), (25) has a unique solution provided that the sampling points (u_i, v_i, \mathbf{p}_i) satisfy the Schoenberg-Whitney condition [36]. This means that for each $[\zeta_i^u, \zeta_{i+k}^u] \times [\zeta_j^v, \zeta_{j+k}^v]$ there must exist at least one sample point (u_z, v_z, \mathbf{p}_z) such that $\zeta_i^u < u_z < \zeta_{i+k}^u$ and $\zeta_j^v < v_z < \zeta_{j+k}^v$.*

Notice that the above process can of course also be used for the determination of a NURBS curve from a set of points. The determination of all NURBS patches is now done as follows. First, find all separating curves \mathcal{C}_i and compute the four NURBS curves \mathbf{K}_1^u , \mathbf{K}_2^u , \mathbf{K}_1^v , and \mathbf{K}_2^v by the above algorithm. The NURBS curves should fulfill the compatibility conditions in (20). Afterwards, determine the NURBS surface which interpolates those four curves by solving the minimization problem (23).

For the numerical solution of boundary integral equations all patches should have a *positive* orientation which implies that on all patches the normal vector points outward the molecule. If adjacent NURBS patches are oriented in the same direction, then their common edge is traversed from both sides in opposite directions. As a consequence, starting from one patch, we can flip the orientation of the patches by redefining the control points and weights according to $\mathbf{d}_{i,j} := \mathbf{d}_{j,i}$ and $w_{i,j} := w_{j,i}$ until all patches have the same direction. To check whether the final orientation is positive or not, we compute the volume of the molecule by the Gauss theorem

$$V(\Omega) = \int_{\Omega} 1 d\mathbf{x} = \frac{1}{3} \int_{\Gamma} \langle \mathbf{n}, \mathbf{x} \rangle d\sigma.$$

If the computed volume is negative, then the normal points in the wrong direction and the orientation is negative.

6 Numerical results

6.1 Cavity generation

In this section, we present results of the cavity generation. To get a first impression, in Figs. 9 and 10 we visualized the graphical output for a DNA molecule and a water cluster, respectively. Next, we report on some numerical tests related with the runtime of the cavity generation. The runtime depends on several factors, namely on the number and the distribution of the molecule's atoms as well as on the coarseness of the patch decomposition.

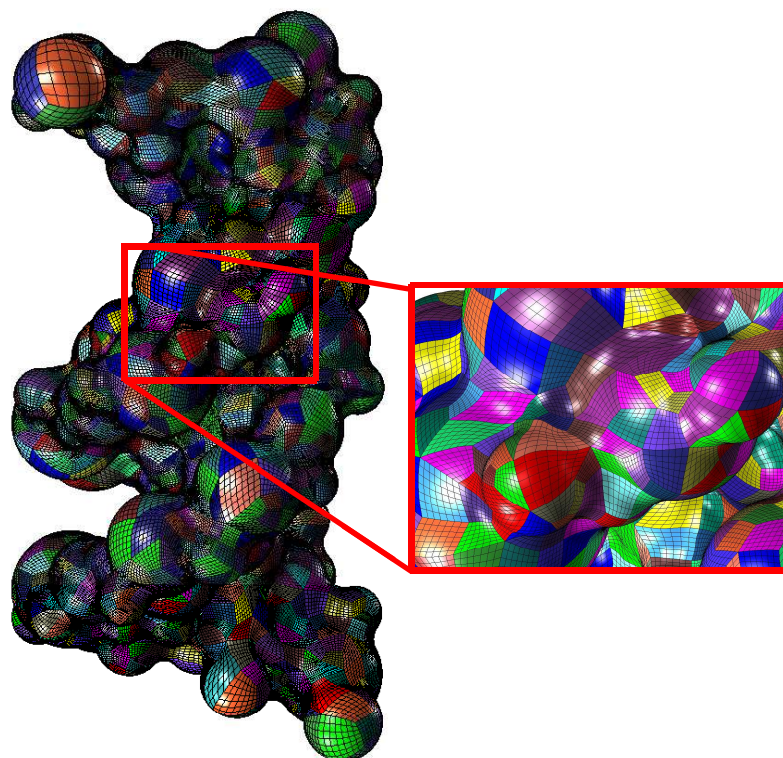


Fig. 9 Patch representation of a DNA with 1905 NURBS.

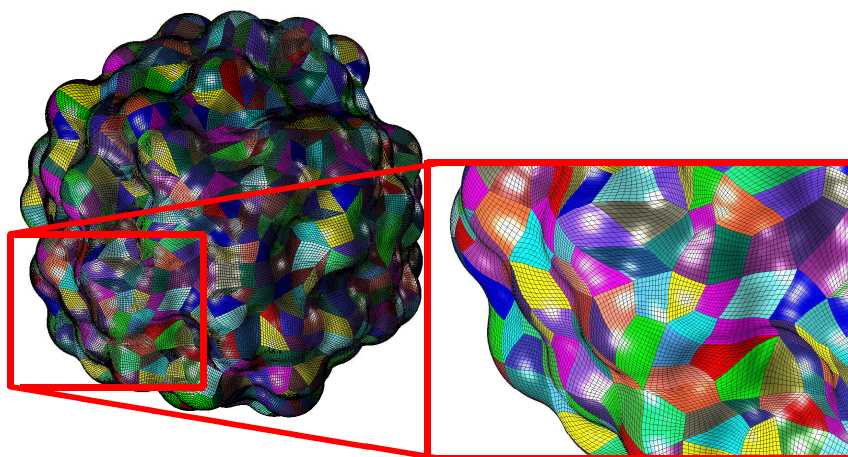


Fig. 10 Patch representation of a water cluster with 1089 NURBS.

Our first numerical test is concerned with the number of patches relative to the number of atoms of the molecule. The results of this test are tabulated in Tab. 2. According to our experience, the interesting practical values of the *coarseness factor* α range between 0.2 and 0.4. The choice $\alpha = 1$ means no coarsening, i.e., $Q_{\text{coarse}} = Q_{\text{fine}}$ (see Subsect. 4.2), whereas $\alpha = 0$ is the coarsest quadrangulation which can be generated by our algorithm. A small value of α amounts to a fewer number of fitting tasks. On the other hand, a single large NURBS surface area needs many sampling points. This means that it takes more time to complete the NURBS determination. The runtime depends therefore not

only on the initial molecular size but also on the surface area of the cavity. For example, lecithin has more atoms than DNA but the cavity generation of DNA takes almost four times longer.

molecules	#atoms	#patches (runtime in seconds)		
		$\alpha = 0.2$	$\alpha = 0.3$	$\alpha = 0.4$
benzene	12	84 (13.86 s)	97 (14.06 s)	119 (14.60 s)
cyclohexane	18	99 (15.27 s)	108 (16.27 s)	127 (16.13 s)
LDS	49	286 (50.36 s)	346 (53.73 s)	409 (52.76 s)
streptomycin	81	399 (68.69 s)	468 (67.78 s)	564 (74.02 s)
lecithin	128	687 (118.50 s)	821 (120.68 s)	932 (145.11 s)
PDMPG	225	1102 (219.23 s)	1345 (219.12 s)	1556 (226.34 s)
DNA	116	1610 (461.67 s)	1899 (475.33 s)	2232 (487.38 s)

Table 2 Number of patches relative to the number of atoms and the coarseness factor α .

The purpose of the second test is the investigation of the size $|I_i|$ of each patch I_i . We compare the areas of the patches with respect to two perspectives, a local and a global comparison. For the local test, let \mathcal{N}_i denote the set of neighboring patches which have at least one vertex in common with the patch I_i . We compute the ratios

$$M(i) := |I_i| / \left(\frac{1}{\text{card}(\mathcal{N}_i)} \sum_{j \in \mathcal{N}_i} |I_j| \right)$$

and tabulate their mean in the third column of Tab. 3. One figures out that the sizes of the patches vary slowly because $M(i)$ approximates the unity. The size and the shape of the patches of SES surfaces are in general very nice. This fact is a clear advantage of the SES surfaces over the van der Waals surface [20] where the patches are located on single atoms and may have extremely varying sizes.

molecules	#patches	area/neighboring area	area/ideal area
benzene	12	0.960095	0.706800
cyclohexane	97	0.959639	0.695809
tamoxifen	410	1.012924	0.665099
streptomycin	462	0.959130	0.662762
lecithin	821	0.971143	0.676250
PDMPG	2175	1.015307	0.688102
DNA	3144	0.950066	0.651584

Table 3 Investigation of the patches area.

The ideal area μ_{ideal} of a patch is the area of the whole molecular surface divided by the number of all patches. Hence, for the global comparison, we compute for each patch I_i the ratio

$$R(i) := \min \left\{ |I_i| / \mu_{\text{ideal}}, \mu_{\text{ideal}} / |I_i| \right\} \in [0, 1].$$

The mean of the values of $R(i)$ is found in the last column of Tab. 3. We observe that the sizes of the patches differ not too much from the ideal size. In fact, we generally have $|I_i| = \rho \mu_{\text{ideal}}$ (or vice versa $\mu_{\text{ideal}} = \rho |I_i|$) with a factor $\rho \in [0.65, 0.75]$.

Our last test consists in investigating the patch quality. Let $\mathbf{a}, \mathbf{b}, \mathbf{c}, \mathbf{d}$ denote the four vertices of a given element $I_{i,j,\mathbf{k}}$ (see Subsect. 2.6). Let $\theta(T_\ell)$ denote the smallest angle in the triangle T_ℓ , $\ell = 1, 2, 3, 4$, defined by

$$T_1 := [\mathbf{a}, \mathbf{b}, \mathbf{c}], \quad T_2 := [\mathbf{a}, \mathbf{c}, \mathbf{d}], \quad T_3 := [\mathbf{a}, \mathbf{b}, \mathbf{d}], \quad T_4 := [\mathbf{b}, \mathbf{c}, \mathbf{d}].$$

In order to quantify the quality of the element $I_{i,j,\mathbf{k}}$ we introduce the measure

$$\Psi(I_{i,j,\mathbf{k}}) := \frac{1}{2} \left[\min \{ \theta(T_1), \theta(T_2) \} + \min \{ \theta(T_3), \theta(T_4) \} \right].$$

molecules	#patches	Ψ -value	
		average	ratio with Ψ_{ideal}
benzene	133	0.595737	0.758516
quinine	358	0.554006	0.705383
borane	812	0.531560	0.676803
lecithin	821	0.555027	0.706682
water cluster	1567	0.571700	0.727911
DNA	3348	0.576848	0.734465

Table 4 Quality of the resulting patches.

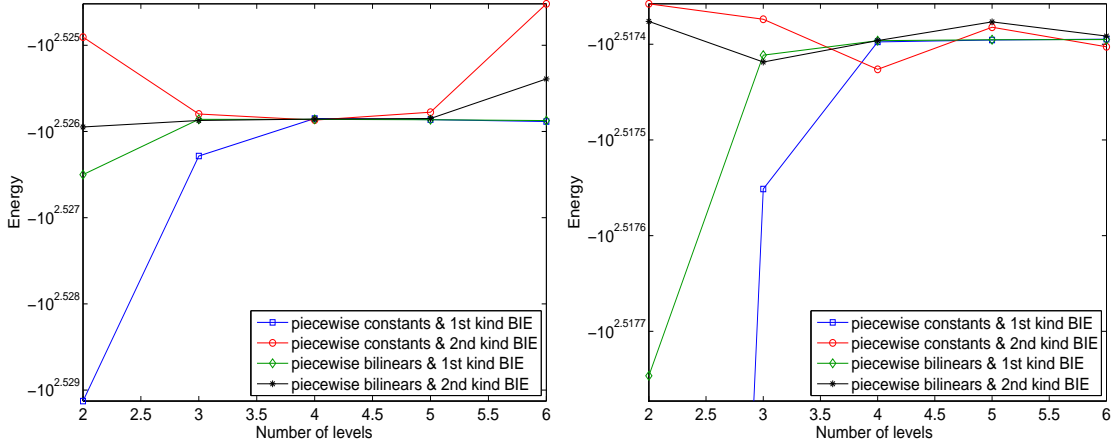


Fig. 11 Interaction energies in case of a VWS (left) and SES (right) surface of benzene.

The ideal element is a square and corresponds to $\Psi_{\text{ideal}} = \pi/4 \approx 0.785398$. In general, it is impossible to attain always the ideal value since not all patches could be a squares. Whereas, a small value of Ψ indicates a bad quad quality. In Tab. 4, for $j = 5$, we gather the results of our tests which consists in computing the average values of Ψ for all elements. We also listed the ratio of these value and the ideal value Ψ_{ideal} .

6.2 Wavelet BEM

In contrast to the SAS/VWS surface the molecule's SES surface is smooth. Therefore, it is worthwhile to discretize the underlying boundary integral equations (5), (6) and (7) by piecewise bilinear boundary elements instead of using the standard piecewise constant approximation. Moreover, in case of original PCM, the convergence of the Galerkin approximation of the second kind integral equation (7) is ensured since the double layer operator is compact.

To validate these statements we compare the results of piecewise constant and bilinear boundary elements in case of benzene. Its VWS surface is represented by 160 patches (we refer the reader to [20] for the construction of the parametrization), whereas the SES surface requires only 91 patches. We place point charges at the nuclei positions and are interested in the interaction energy

$$E_I(\rho, \rho) = -\frac{1}{2} \int_{\Gamma} \sigma \mathcal{N}_{\rho} d\omega.$$

Water at 25° Celsius is considered as solvent which leads to original PCM with $\kappa = 0$ and $\underline{\varepsilon} = 78.39$. The apparent surface charge is computed by the respectively first and second kind integral equations (6) and (7). In Fig. 11 we plotted the approximate exchange energies.

We figure out that for both types of surfaces bilinear boundary elements converge much faster to the energies -335.64 (VWS surface) and -329.15 (SES surface). The energies are of course different

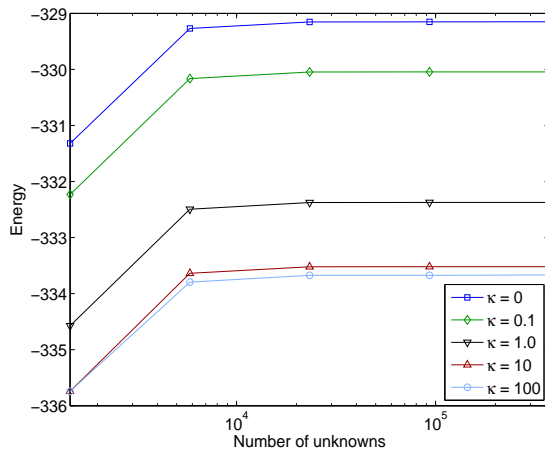


Fig. 12 Interaction energy in dependence on the Debye length.

level	a-priori compression (in/exterior)	a-posteriori compression (interior)	a-posteriori compression (exterior)				
			$\kappa = 0$	$\kappa = 0.1$	$\kappa = 1$	$\kappa = 10$	$\kappa = 100$
2	13 %	10 %	10 %	10 %	8.6 %	2.3 %	1.5 %
3	5.6 %	3.3 %	3.3 %	3.3 %	2.7 %	1.0 %	0.71 %
4	1.8 %	0.76 %	0.76 %	0.76 %	0.69 %	0.37 %	0.23 %
5	0.53 %	0.19 %	0.19 %	0.19 %	0.18 %	0.12 %	0.068 %
6	0.14 %	0.050 %	0.050 %	0.050 %	0.046 %	0.0344 %	0.021 %

Table 5 Compression rates in dependence on the Debye length.

since the surfaces differ. In case of the VWS surface and the second kind integral equation (7) the energy starts to diverge on higher levels which issues from the fact that the double layer operator is not compact. On SES surfaces the boundary element method provides higher accuracy and faster convergence (seen by the different scaling of the y -axes). The first kind integral equation is superior to the second kind integral equation.

Next, we like to study the influence of an ionic solvent, i.e., the dependence on the Debye length $1/\kappa$. Due to $\kappa \neq 0$ we have now to solve the boundary integral equation (5), i.e., we need to assemble four integral operators instead of two like in original PCM. We apply a piecewise constant discretization of the apparent surface charge. In accordance with Fig. 12 we observe that the convergence is not affected by the different values of κ . However, the interaction energy decreases as κ increases, where the energy becomes less sensitive with respect to κ for large values of κ .

We finally present the compression rates of the wavelet matrix compression. The relative number of nonzero coefficients is tabulated in Tab. 5. The exterior double and single layer operators become more and more local as κ increases. This is confirmed by the a-posteriori compression rates of the related system matrices. In our implementation we do so far not exploit this fact, that is, the compression pattern of all system matrices are computed like in the case of the pure Laplacian. Nevertheless, on level 6 less than 580 coefficients per degree of freedom remain in the mean after the a-priori compression.

References

1. C. Bajaj, G. Xu, and Q. Zhang. A fast variational method for the construction of adaptive resolution C^2 smooth molecular surfaces. *Comput. Methods Appl. Mech. Eng.* **198**, 1684–1690 (2009).
2. H. Bast, K. Mehlhorn, G. Schäfer, and H. Tamaki. A heuristic for Dijkstra’s algorithm with many targets and its use in weighted matching algorithms. *Algorithmica* **36**, 75–88 (2003).
3. G. Beylkin, R. Coifman, and V. Rokhlin. The fast wavelet transform and numerical algorithms. *Comm. Pure and Appl. Math.* **44**, 141–183 (1991).

4. G. Brunnett. Geometric design with trimmed surfaces. *Comput. Suppl.* **10**, 101–115 (1995).
5. E. Cancés and B. Mennucci. New applications of integral equations methods for solvation continuum models: ionic solutions and liquid crystals. *J. Math. Chem.* **23**, 309–326 (1998).
6. E. Cancés, B. Mennucci, and J. Tomasi. A new integral equation formalism for the polarizable continuum model: Theoretical background and applications to isotropic and anisotropic dielectrics. *J. Chem. Phys.* **107**, 3032–3041 (1997).
7. H.L. Cheng and X. Shi. Quality mesh generation for molecular skin surfaces using restricted union of balls. *Comput. Geom.* **42**, 196–206 (2009).
8. M. Connolly. Analytical molecular surface calculation. *J. Appl. Cryst.* **16**, 548–558 (1983).
9. M. Connolly. Molecular surface guide. <http://connolly.best.vwh.net> (2006).
10. W. Dahmen, H. Harbrecht, and R. Schneider. Compression techniques for boundary integral equations — optimal complexity estimates. *SIAM J. Numer. Anal.* **43**, 2251–2271 (2006).
11. W. Dahmen and A. Kunoth. Multilevel preconditioning. *Numer. Math.* **63**, 315–344 (1992).
12. H. Edelsbrunner and N.R. Shah. Incremental topological flipping works for regular triangulations. *Algorithmica* **15**, 223–241 (1996).
13. B. Elsässer. *Approximation mit rationalen B-Spline Kurven und Flächen*. PhD thesis, Technische Universität Darmstadt (1998).
14. L. Frediani, R. Cammi, S. Corni, and J. Tomasi. A polarizable continuum model for molecules at diffuse interfaces. *J. Chem. Phys.* **120**, 3893–3907 (2004).
15. J. Gallier. *Geometric methods and applications for computer science and engineering*. Springer, New York (2001).
16. L. Greengard and V. Rokhlin. A fast algorithm for particle simulation. *J. Comput. Phys.* **73** 325–348, (1987).
17. W. Hackbusch and B.N. Khoromskij. A sparse \mathcal{H} -matrix arithmetic. II: Application to multi-dimensional problems. *Computing* **64**, 21–47 (2000).
18. W. Hackbusch and Z.P. Nowak. On the fast matrix multiplication in the boundary element method by panel clustering. *Numer. Math.* **54**, 463–491 (1989).
19. H. Harbrecht and M. Randrianarivony. From computer aided design to wavelet BEM. *Comput. Vis. Sci.* **13**, 69–82 (2010).
20. H. Harbrecht and M. Randrianarivony. Wavelet BEM on molecular surfaces: parametrization and implementation. *Computing* **86**, 1–22 (2009).
21. H. Harbrecht and R. Schneider. Biorthogonal wavelet bases for the boundary element method. *Math. Nachr.* **269–270**, 167–188 (2004).
22. H. Harbrecht and R. Schneider. Wavelet Galerkin Schemes for boundary integral equations – implementation and quadrature. *SIAM J. Sci. Comput.* **27**, 1347–1370 (2002).
23. J. Hoschek and D. Lasser. *Fundamentals of computer aided geometric design*. A.K. Peters, Wellesley (1993).
24. P. Laug and H. Borouchaki. Molecular surface modeling and meshing. *Eng. with Comp.* **18**, 199–210 (2002).
25. B. Lee and F. Richards. The interpretation of protein structures estimation of static accessibility. *J. Mol. Biol.* **55**, 379–400 (1971).
26. S. Miertuš, E. Scrocco, and J. Tomasi. Electrostatic interaction of a solute with a continuum. A direct utilization of ab initio molecular potentials for the prevision of solvent effects. *Chem. Phys.* **55**, 117–129 (1981).
27. L. Pirlgl and W. Tiller. *The NURBS book*. Springer, Berlin (1995).
28. J.L. Pascual-ahuir, E. Silla, and I. Tuñón. GEPOL: An improved description of molecular surfaces. III. A new algorithm for the computation of a solvent-excluding surface. *J. Comput. Chem.* **15**, 1127–1138 (1994).
29. C. Pomelli. A tessellationless integration grid for the polarizable continuum model reaction field. *J. Comput. Chem.* **25**, 1532–1541 (2004).
30. M. Randrianarivony. *Geometric processing of CAD data and meshes as input of integral equation solvers*. PhD thesis, Technische Universität Chemnitz (2006).
31. M. Randrianarivony. On global continuity of Coons mappings in patching CAD surfaces. *Comput.-Aided Design* **41**, Springer, Berlin-Heidelberg, pp. 782–791 (2009).
32. M. Randrianarivony and G. Brunnett. Molecular surface decomposition using graphical modeling. in *Bildverarbeitung für die Medizin: Algorithmen — Systeme — Anwendungen*, Proceedings des

- Workshops vom 6. bis 8. April 2008 in Berlin, Springer, Berlin-Heidelberg, pp. 197–201 (2008).
33. M. Randrianarivony. Harmonic variation of edge size in meshing CAD geometries from IGES format. *Lect. Notes Comput. Sci.* **5102**, 56–65 (2008).
 34. M. Sanner, A. Olsen, and J. Spehner. Reduced surface: an efficient way to compute molecular surfaces. *Biopolymers* **38**, 305–320 (1996).
 35. S. Sauter and C. Schwab. *Randelementmethoden: Analyse, Numerik und Implementierung schneller Algorithmen*. Teubner, Stuttgart (2004).
 36. L. Schoenberg and A. Whitney. On Polya frequency functions III. *Trans. Amer. Math. Soc.* **74** 246–259 (1953).
 37. J. Tomasi, B. Mennucci, and R. Cammi. Quantum mechanical continuum solvation models. *Chem. Rev.* **105** 2999–3094 (2005).
 38. U.S. Product Data Association. *Initial graphics exchange specification. IGES 5.3*. Trident Research Center, SC (1996).
 39. V. Weijo, M. Randrianarivony, H. Harbrecht, and L. Frediani. Wavelet formulation of the polarizable continuum model. *J. Comput. Chem.* **31**, 1469–1477 (2010).
 40. D. Whitley. Van der Waals graphs and molecular shape. *J. Math. Chem.* **23**, 377–397 (1998).